Journal of Materials Chemistry A

Unveiling the role of hydrothermal carbon dots as anodes in sodium-ion batteries with ultrahigh initial Coulombic efficiency

Journal:	*Journal of Materials Chemistry A*
Manuscript ID	TA-ART-10-2019-011369.R1
Article Type:	Paper
Date Submitted by the Author:	03-Nov-2019
Complete List of Authors:	Xie, Fei; Queen Mary University of London, School of Physics and Astronomy; Imperial College London, Department of Chemical Engineering Xu, Zhen; Imperial College London, Department of Chemical Engineering Jensen, Anders; Queen Mary University of London Ding, Feixiang; Chinese Academy of Sciences Institute of Physics Au, Heather; Imperial College London, Chemical Engineering Feng, Jingyu; Imperial College London Luo, Hui; Queen Mary University of London, School of Engineering and Materials Science Qiao, Mo; Imperial College London, Chemical Engineering Guo, Zhenyu; Imperial College London, Department of Chemical Engineering Lu, Yaxiang; Institute of Physics, Chinese Academy of Sciences, Drew, Alan; Queen Mary University of London, School of Physics and Astronomy Hu, Yong-Sheng; Institute of Physics, Chinese Academy of Sciences, Titirici, Magdalena; Imperial College London, Department of Chemical Engineering; Queen Mary University of London, School of Engineering and Materials Science

Table of content

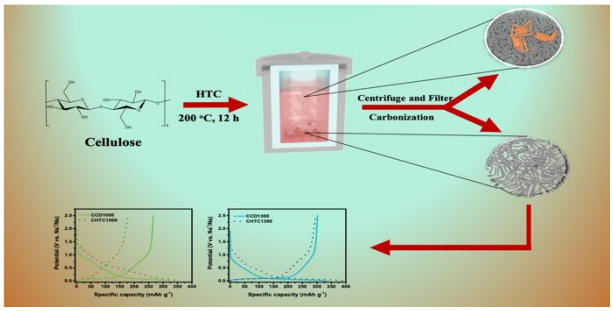

We report the discovery of usually ignored hydrothermal carbon dots as anodes in sodium-ion batteries with ultrahigh initial Coulombic efficiency

ARTICLE

Unveiling the role of hydrothermal carbon dots as anodes in sodium-ion batteries with ultrahigh initial Coulombic efficiency

Received 00th January 20xx,
Accepted 00th January 20xx

DOI: 10.1039/x0xx00000x

Fei Xie,[a,b] Zhen Xu,[a] Anders C. S. Jensen,[a,b] Feixiang Ding,[d] Heather Au,[a] Jingyu Feng,[a] Hui Luo,[a,c] Mo Qiao,[a] Zhenyu Guo,[a] Yaxiang Lu,[d] Alan J. Drew,[b] Yong-Sheng Hu[d] and Maria-Magdalena Titirici*[a]

Hard carbon materials are regarded as the most promising anode materials for sodium-ion batteries (SIBs) due to their best cost-effectiveness. However, the relatively low specific capacity and initial Coulombic efficiency (ICE) compared with the graphite anode in lithium-ion batteries still limit the energy density for further development. Thus, it is necessary to produce high-performance hard carbon anode materials with high ICE to improve the SIB technology. Here we show the use of usually ignored carbon dots from the supernatant of hydrothermal carbonization (HTC) as anodes in SIBs after directly drying and carbonization. Compared to the traditional HTC carbon spheres from the solid phase, the further carbonized carbon dots exhibit an excellent specific capacity over 300 mAh g^{-1} with a significantly enhanced ICE up to 91% at 30 mA g^{-1} which is among the highest value of reported carbonaceous anodes in SIBs. The superior ICE could benefit a high energy density of 248 Wh kg^{-1} in full cell with $NaNi_{1/3}Fe_{1/3}Mn_{1/3}O_2$ cathode. This new discovery from the simple traditional method provides new aspects of designing high-performance SIBs in the future commercilization.

Introduction

Sodium-ion batteries (SIBs) are regarded as a very promising emerging alternative to lithium-ion batteries (LIBs) owing to the abundance and wide distribution of Na resources which could better face the increased demand of energy storage today.[1] The use of Al current collectors and lower cost transition metals such as Fe and Mn rather than Co for cathode materials in LIBs further reduces the total cost of SIBs.[2,3] Currently, the absence of proper anode materials with great sodium storage performance is still a main challenge in this field. Wherein, carbonaceous materials have the greatest potential as commercial anode materials for SIBs because of their low cost, sustainability, structural stability and good performance. However, the relatively low ICE is still not competitive with the graphite anode in lithium-ion batteries. Only a few literatures reported the ICE of carbon materials in SIBs which could be over 90%,[4,5] significantly limiting the energy density and future commercialization.[6] Therefore, designing high-performance carbonaceous anode materials with high ICE is a necessary task among the research topics for next-generation SIBs.

A class of new carbon materials named carbon dots with very small (less than 10 nm in size) crystalline carbon nanoparticles with unique optical properties has gradually attracted people's attentions and has been widely used for extending the light absorption as well as tuning the band gap of semiconductors and applied to photocatalysis and solar cells.[7–10] Although a few papers have reported the use of carbon dots as anodes in SIBs,[11] the chemical synthesis method is relatively complicated and noneconomical which may limit the practical commercialization in SIBs. Furthermore, when used as electrodes, only sloping regions were present in the discharge/charge curves with low ICE, which extensively suppress the energy density.

Hydrothermal carbonization (HTC) is a simple established technique to pre-treat the biomass and convert it into sustainable carbon materials. Generally, dehydration of the carbohydrate precursor is followed by polymerization resulting in the nucleation and growth of polyfuranic spheres which upon further carbonization under inert atmosphere form hard carbon microspheres.[12–14] At the same time, the liquid phase remaining after the isolation of these microspheres also contains the carbon dots.[15,16] Previous works have focused on the use of carbon micro/nano sphere solids precepted at the bottom of the HTC vessel as anode materials for SIBs,[17–21] but the carbon dots suspended in the liquid phase were usually ignored. To the best of our knowledge, there has been no study using these hydrothermal carbon dots isolated from the HTC liquid phase for SIB applications.

In this work, cellulose-derived carbon dots (CCDs) from the supernatant of the HTC process as precursors were directly dried and further carbonized, and their electrochemical performance as anodes in SIBs was investigated. Compared to the solid phase-derived HTC carbon spheres commonly employed as anodes in SIBs, the carbonized CCDs show a significantly enhanced ICE with excellent sodium storage capacity due to the lower surface area, fewer defects

[a] Department of Chemical Engineering, Imperial College London, London, SW7 2AZ, UK. Email: m.titirici@imperial.ac.uk
[b] School of Physics and Astronomy, Queen Mary University of London, London, E1 4NS, UK.
[c] School of Engineering and Materials Science, Queen Mary University of London, London, E1 4NS, UK
[d] Beijing Key Laboratory for New Energy Materials and Devices, Beijing National Laboratory for Condensed Matter Physics, Institute of Physics, Chinese Academy of Sciences, Beijing 100190, P. R. China.
Electronic Supplementary Information (ESI) available: [details of any supplementary information available should be included here]. See DOI: 10.1039/x0xx00000x

and higher graphitic degree. Wherein, the CCD carbonized to 1300 °C has a superior ICE of 91%, which is one of the highest values reported for hard carbon anodes in SIBs. The compacted irreversible capacity also lowers the amount of cathode material required, thereby, reducing the overall cost of full cell production and contribute to higher energy density. This discovery that the carbon dots from the liquid phase of the HTC process as high-ICE anodes in SIBs could provide not only more effective utilization of the HTC method when dealing with carbon precursors but also a new aspect of designing promising high-ICE carbon anode materials for practical high-performance SIBs.

Experimental

Materials synthesis

Typically, 1.4 g cellulose powders (Sigma Aldrich, UK) and 35 mL distilled water were mixed in a 50-mL Teflon inlet and put in a stainless autoclave for hydrothermal carbonization (HTC) to 200 °C for 12 h. The entire contents of the vessel were then centrifuged at 10000 rpm for 10 min. The supernatant which contains the carbon dots was filtered through a 0.2 μm syringe filter and then freeze-dried for 3 days with subsequent drying at 80 °C overnight in a vacuum oven. The solid contents from the deposit were centrifuged twice more and dried at 80 °C overnight. The carbonaceous items from both the supernatant and deposit were further carbonized at 1000, 1300, and 1500 °C in a STF tube furnace under N_2 protection for 1 h with a heating rate of 5 °C min^{-1}. The resulting carbon samples from the liquid phase in the supernatant which are the cellulose-derived carbon dots are donated as CCD1000, CCD1300 and CCD 1500, while the ones from the solid phase at the bottom which are cellulose-derived HTC carbons are denoted as CHTC1000, CHTC1300 and CHTC1500.

Materials characterization

The morphologies of carbonized CCDs and CHTCs are observed by using FEI Inspect F scanning electron microscope (SEM). JEOL 2010 transmission electron microscope (TEM) was used to look the turbostratic nanodomains. The photoluminescence properties of the carbon dots were measured on Perkin Elmer LS 55 fluorescence spectrometer. The defect nanostructures of the samples were investigated using a Renishaw InVia Reflex Raman spectrometer with a wavelength of 633 nm. X-ray photoelectron spectroscopy (XPS) was performed on a ThermoFisher Nexsa X-ray spectrometer equipped with an Al-Kα monochromated X-ray source. N_2 adsorption was performed on a Quantachrome NOVA 4200 system.

A Xenocs nano-InXider with a Cu-Kα source was used to perform the small/wide angle X-ray scattering (SAXS/WAXS) and a two-detector setup for combined SAXS/WAXS measurements. The non-sodiated pristine samples were packed in 2 mm Kapton capillaries, while the sodiated samples were packed in 1.5 mm glass capillaries in a glove box and sealed to avoid reaction with air. The SAXS results were analyzed using a Porod method as described by Stevens and Dahn[22] to determine the pore structures and surface areas of the resulting caron samples. The SAXS region could be fitted well with the approach reported by Steve and Dahn's group as follows:[22]

$$I(Q) = \frac{A}{Q^{\alpha}} + \frac{B a_1^4}{(1 + a_1^2 Q^2)^2} + D \quad (1)$$

where the *A* and *B* parameters are proportional to the total surface area of the large and small pores respectively. Q is the scattering vector and α is the slope of the initial drop of the intensity in the logarithmic plot, which indicates the changes in the morphology of the material. D is a constant background term and a_1 is characteristic length over which the scattering power changes and associated with the radius of a spherical pore volume by $R = a_1\sqrt{10}$. To analyze the ex situ SAXS data, the modified Porod equation was used:[22]

$$I(Q) = \frac{A}{Q^{\alpha}} + \frac{B a_1^4 \Delta\rho^2}{(1 + a_1^2 Q^2)^2} + \frac{C}{(1 + a_2^2 Q^2)^2} + D \quad (2)$$

where Δρ represents the electron density contrast, sensitive to changes in the electron density of the pores, which is assumed to be caused by sodiation and can be set to 1 in pristine carbon. a_2 is the characteristic length of an additional intermediate pore size and C is proportional to the surface area of the pores with the intermediate size. The d_{002} were calculated based on XRD patterns by using Bragg equation:[23]

$$d_{002} = \frac{\lambda}{2 sin\theta} \quad (3)$$

where λ is the wavelength of the X-ray (0.154 nm) and θ is the Bragg angle of (002) peaks.

Electrochemical measurements

All the resulting carbon samples were mixed with sodium alginate (Sigma Aldrich, UK) binder (weight ratio: 9.5:0.5) in distilled water. The slurry was then coated onto Al foils to make the electrodes. The loading mass of active materials was controlled between 1.5-2 mg cm^{-1}. All the electrodes were vacuum dried at 120 °C overnight before assembling in CR2032 coin cells in an Ar-filled glovebox (H_2O<0.5, O_2<0.5) and measuring at room temperature. Metallic sodium (Sigma Aldrich, UK) was used as the counter electrode in half cells and $NaNi_{1/3}Fe_{1/3}Mn_{1/3}O_2$ was used as the cathode material for full cells. The mass ratio of the anode and cathode active materials are around 1:2.2 and the size of both electrodes are 8mm in diameter. The cathode material was previously reported in the literature [24] and the charge/discharge profile in half cell is shown in Fig. S13a. GF/D glass fiber (Whatman, UK) was used as the separator. 1 M $NaClO_4$ in ethylene carbonate (EC) and dimethyl carbonate (DMC) (1:1, v/v) was selected as the electrolyte for half cells, while 1 M $NaPF_6$ in EC and diethyl carbonate (DEC) (1:1 v/v) for the full cells. All the half cells are discharge/charged between 0-2.5 (V vs. Na^+/Na), while the full cells are tested within the voltage window of 0-4 V. Galvanostatic charge/discharge, rate and cycling capability, and galvanostatic intermittent titration technique (GITT) were performed on LAND CT2001A battery testing system. The diffusion coefficient of Na^+ ions *D* is calculated from GITT results based on Fick's second law:[25,26]

$$D = \frac{4}{\pi\tau}\left(\frac{m_B V_M}{M_B S}\right)^2 \left(\frac{\Delta E_S}{\Delta E_\tau}\right)^2 \quad (4)$$

where τ is the duration of the discharge current; m_B, M_B and V_M is the mass, molar mass and molar volume of the active material; S is the area of the electrodes; ΔE_s is the voltage change between steady stage while $\Delta E\tau$ is the voltage change due to the pulse current. The cyclic voltammetry (CV) and electrochemical impedance spectroscopy (EIS) were measured on an Autolab PGSTAT204 electrochemistry workstation. The capacitive contribution was calculated based on the following equation:[27,28]

$$\mathbf{i(V)} = \boldsymbol{k_1 v} + \boldsymbol{k_2 v^{1/2}} \quad (5)$$

where i(V) is the current at a specific voltage on the CV curve and ν is the scan rate. $k_1\nu$ represents the capacitive behavior while $k_2\nu^{1/2}$ represents the diffusion-controlled process.

Results and discussion

Materials characterizations

The resulting cellulose-derived carbon dots (CCD) and HTC carbons (CHTC) were carbonized at 1000, 1300 and 1500 °C and denotated as CCDT and CHTCT (where T is the pyrolysis temperatures). Fig. 1 shows the scheme of the synthesis of carbonized CCDs and CHTCs, where the CCDs are isolated from the supernatant while the CHTCs are from the solid phase at the bottom. The transmission electron microscopy (TEM) images of CCDs before further carbonization are shown in Fig. S1a-b, suggesting that the carbon dots are some nanodomains with local graphitic nanostructures, embedding on the amorphous carbon layer during the HTC process. Fig. S1c shows the typical florescent properties of CCD, which also confirm the formation of carbon dots upon HTC procedure.

The scanning electron microscopy (SEM) images of the carbonized CCDs and CHTCs (Fig. 1a-b and Fig. S2) indicate that even though CCDs and CHTCs are derived from the same precursor and produced during the same process, the morphologies of these two materials are very different. The carbonized CHTCs have a spherical morphology characteristic of hydrothermal carbons,[12,29] whereas the carbonized CCDs exhibit a structure more typical of directly pyrolyzed amorphous carbons. TEM images show that whilst both CCD1300 and CHTC1300 are composed of predominantly amorphous and turbostratic domains, CCD1300 also contains small local graphitic nanodomains, which are thought to be the carbon dots embedded onto the amorphous carbon during the HTC process, and remained after pyrolysis (Fig. 2c-e). The TEM images of the samples carbonized at 1000 and 1500 °C are shown in Fig. S3, which also demonstrates the embedded carbon dots are visible on the amorphous carbon background, indicating that the nanostructures could be remained at all of the carbonization temperatures. It is worth noting that even the local graphitic domains could be seen in the carbonized CCD samples, the overall turbostratic nanodomains imply that they are still amorphous carbons.

X-ray diffraction (XRD) measurements were performed to investigate the microstructures of carbonized CCD and CHTC samples (Fig. 3a and Fig. S4). There are two broad peaks centered at around 24° and 44° corresponding to the (002) and (100) planes of expanded graphite, respectively, which are typical for disordered carbonaceous materials. The (002) peak of CCD1300 is located at a higher angle compared to CHTC1300, indicating the smaller average interlayer spacing. Also, the sharper and narrower (002) and (100) peaks of CCD1300 (Table S1) demonstrate the relatively larger ordered nanodomains which is in good agreement with the TEM measurements. When the carbonization temperature increases from 1000 °C to 1500 °C, the (002) peaks of the resulting carbons all shift to higher angles and become sharper and narrower, suggesting larger graphitic planes and shorter interlayer spacing. At each temperature, the carbonized CCDs have narrower (002) peaks, and

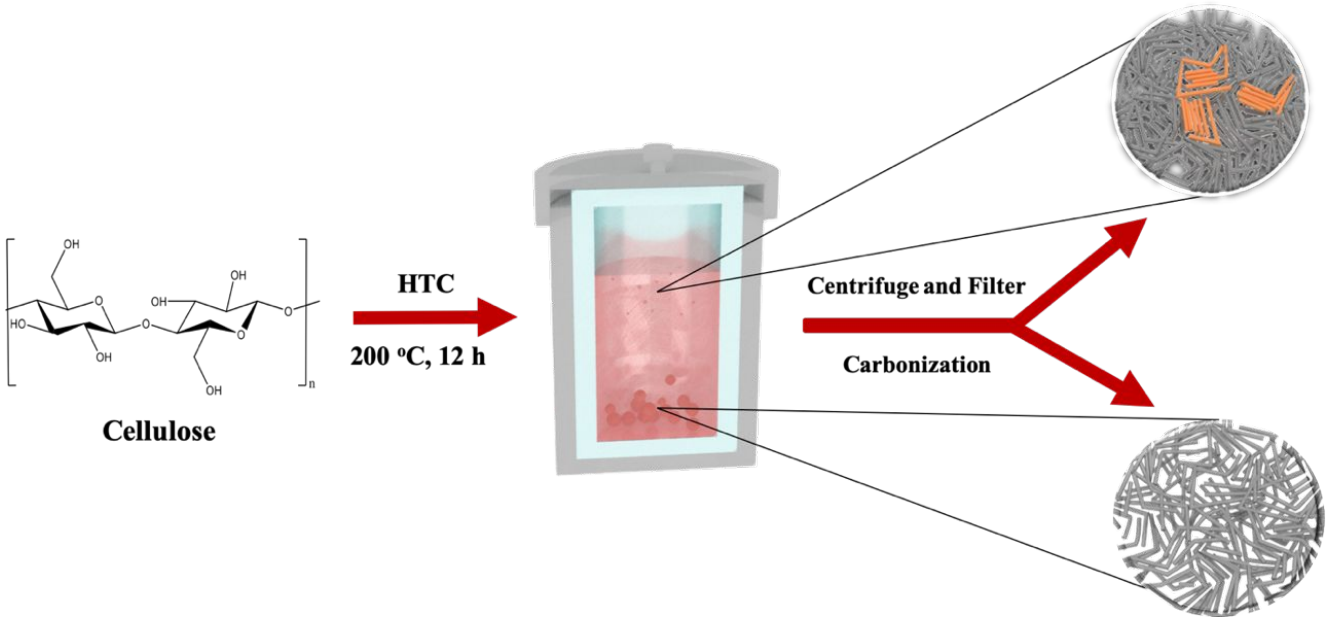

Fig. 1 Scheme illustration of the synthesis of carbonized CCDs and CHTCs.

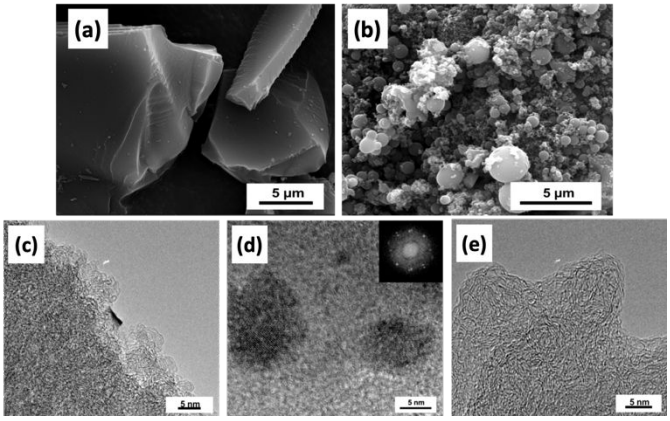

Fig. 2. SEM images of (a) CCD1300; (b) CHTC1300. TEM images of (c) CCD1300; (d) some local graphitic nanodomains in CCD1300 (inset is FFT graph showing the crystallinity); (e) CHTC1300.

shorter interlayer spacing, showing more ordered domains compared with the CHTCs carbonized at the same temperatures.

Raman spectroscopy further reveals the defects in carbonized CCDs and CHTCs. The fitted Raman profiles show the typical D- and G-peaks located at around 1340 and 1580 cm^{-1}.[30] The CCD1300 has sharper peaks and higher I_D/I_G ratio than CHTC1300 (Fig. 3b-c, Table S1). This means that CHTC1300 has a greater number of defects within the graphitic layers and a higher degree of disorder according to the three-stage Raman model proposed by Ferrari *et al*.[31] Higher I_D/I_G ratios are present in carbonized CCD compared with CHTC samples also at carbonization temperatures of 1000 °C and 1500 °C (Fig. S5, Table S1), indicating that fewer defects are present within the graphitic layers of carbonized CCDs compared to CHTCs at all three carbonization temperatures. In addition, for both CCD and CHTC series, the D and G bands sharpen and narrow, and the I_D/I_G ratios increase with increased pyrolysis temperatures, resulting in less disorder, consistent with the previous report.[32]

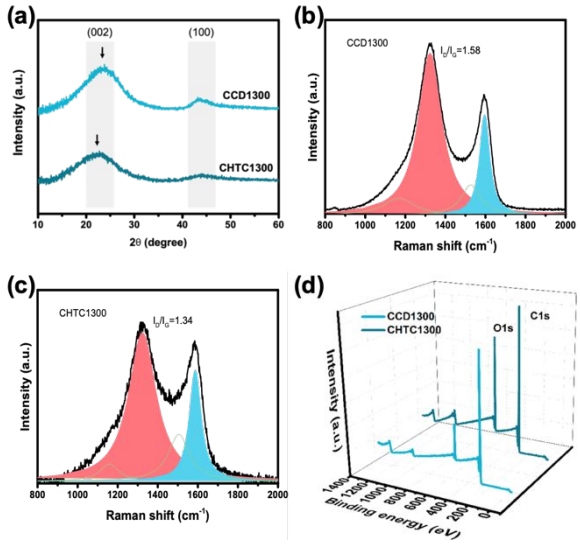

Fig. 3. (a) XRD patterns of CCD1300 and CHTC1300. (b)-(c) Raman spectra of CCD1300 and CHTC1300. (d) XPS survey of CCD1300 and CHTC1300.

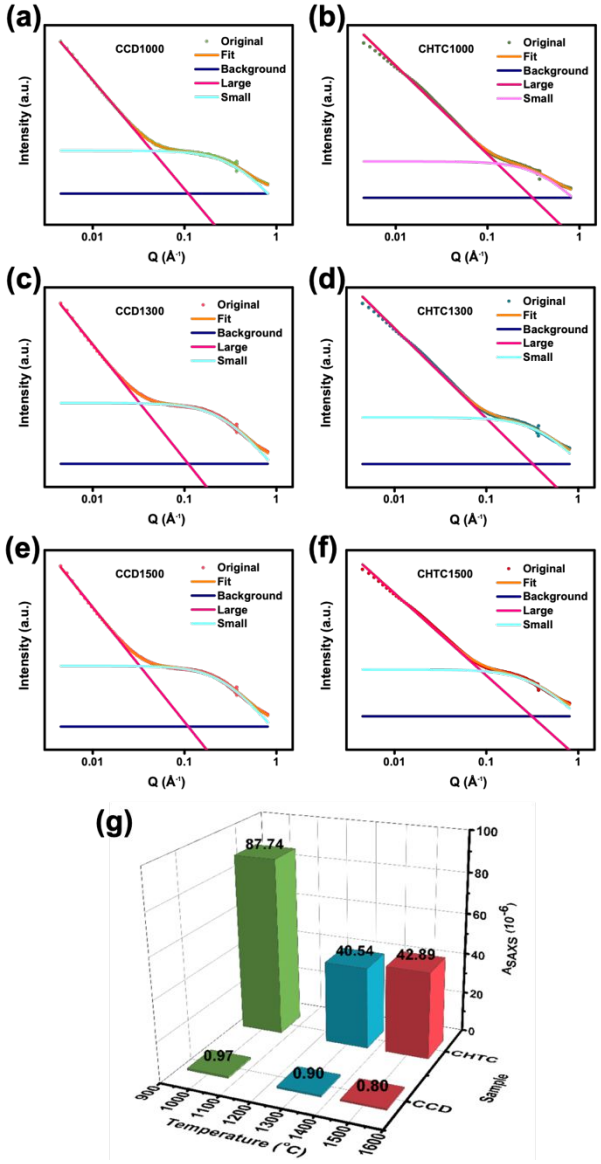

Fig. 4. Fitted SAXS patterns of (a) CCD1000; (b) CHTC1000; (c) CCD1300; (d) CHTC1300; (e) CCD1500 and (f) CHTC1500. (g) A parameter calculated from SAXS results for CCD and CHTC at different carbonization temperatures.

X-ray photoelectron spectroscopy (XPS) was employed to observe the surface functional groups and the elemental composition of the resulting carbons. The XPS survey and fitted C1s peaks are shown in Fig. 3d and Fig. S6. Carbonized CHTC has a much higher oxygen content than CCD at each temperature, suggesting more topological defects.[33,34] The lower oxygen content in CCD may be due to the highly ordered nanodomains which promote oxygen decomposition during the carbonization procedure allowing the surrounding carbon atoms to diffuse to the graphitic domains and form ordered microstructures.[35] The two peaks at around 284.5 and 285.2 eV in the fitted C1s spectra correspond to sp^2 and sp^3 hybridized carbon atom, and the ratio of sp^2 carbon atoms for the carbonized CCDs are higher than the carbonized CHTCs at the same temperatures, while the ratios of sp^3 are higher for the CHTCs (Fig. S6), which confirms

again that the carbonized CCD samples have a more ordered structure than the CHTC samples.[18,35]

Small-angle X-ray scattering (SAXS) was performed to investigate the pore structures and specific surface area of the obtained carbon materials and the fitted profiles based on Porod equation are shown in Fig. 4a-f. An initial slope at low Q shown in each SAXS pattern represents the macroscopic particles and large pores, while a shoulder at intermediate Q represents the nanopores formed between the turbostratic nanodomains.[36] The *A* parameters calculated based on the fittings are proportional to the total surface area from the macroscopic large pores,[22] and the values of all the resulting carbonized CCD and CHTC samples are shown in Fig. 4g. The *A* values of carbonized CHTCs are 87.74, 40.54 and 42.89, respectively, which are much higher than that of the carbonized CCDs (<1) at the same temperatures, indicating much larger specific surface areas of CHTCs compared to CCDs. N_2 adsorption was also performed to compare the surface area of carbonized CCD and CHTC samples (Fig. S7). The same trend of the Brunauer–Emmett–Teller (BET) surface area according to the N_2 adsorption results also indicated that carbonized CHTCs have larger surface areas than the carbonized CCDs, which is consistent with the SAXS results. The calculated pore structure parameters from both SAXS and N_2 adsorption are shown in Table S2.

Overall, the above characterizations demonstrate that the carbonized CCDs show more ordered long-range nanodomains and fewer defects compared to carbonized CHTCs, and the CCD samples have a much smaller specific surface area than the CHTC samples.

Electrochemical performance

To investigate the electrochemical properties, the carbon electrodes were first assembled in half cells with metallic sodium as the counter electrode. Fig. 5a-b and Fig. S8a show the initial galvanostatic discharge/charge curves of CCD and CHTC carbonized at different temperatures at a current density of 30 mA g^{-1}. Clearly, the carbonized CCDs have much lower irreversible capacity at the first cycles. The initial Coulombic efficiencies (ICE) of CCD1000, CCD1300 and CCD1500 are 82%, 91% and 89% respectively, which are much higher than those of the corresponding CHTC samples (50%, 75% and 76%), where CCD1300 has one of the highest ICE reported for carbonaceous anode materials in SIBs (Table S3) and is competitive to the graphite anode in commercial lithium-ion batteries. This could be attributed to the condensed stacking morphology and lower specific surface area of carbonized CCD samples which reduce the contact area between electrode and electrolyte and allows the formation of a less solid electrolyte interphase (SEI).[37] At the same time, the more ordered nanostructure, lower amount of oxygen groups and defects trap fewer Na^+ ions with high binding energy and therefore cause less irreversibility in the first cycle,[30,35,38–40] also resulting in the higher ICE of carbonized CCD samples. In the case of CHTC1000, the high surface area and low graphitic level causes a significant Na^+ ion consumption leading to an extensive SEI formation which significantly limits the utilization of sodium storage sites within the electrode and leads to a very low reversible capacity of only 178 mAh g^{-1}. Conversely, the lower surface area and more ordered

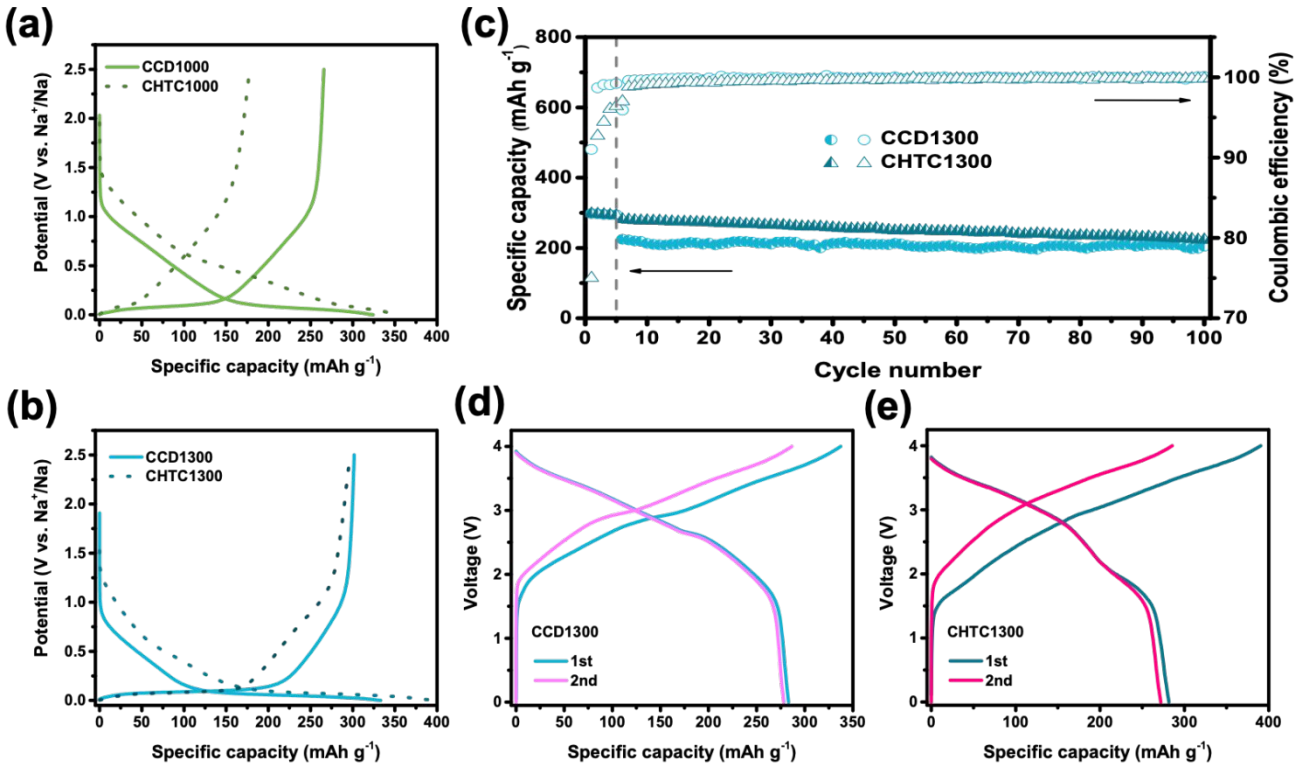

Fig. 5. (a)-(b) Initial galvanostatic discharge/charge profiles of CCD and CHTC carbonized at 1000 and 1300 °C at a current density of 30 mA g^{-1} in half cell. (c) Cycling performance of CCD1300 and CHTC1300 at 150 mA g^{-1} in half cell (the first five cycles are performed at 30 mA g^{-1}). (d)-(e) Galvanostatic discharge/charge curves of CCD1300 and CHTC1300 paired with $NaNi_{1/3}Fe_{1/3}Mn_{1/3}O_2$ cathode in coin type full cell at 30 mA g^{-1}.

structures of CCD1000 increases its reversible capacity to 266 mAh g^{-1}. CCD1300 and CHTC1300 have the comparable high reversible capacity of 302 and 297 mAh g^{-1}, respectively, but the much higher ICE of CCD1300 makes this material a more promising anode for SIBs. The too high graphitic level of CCD1500 makes its capacity lower than CHTC1500, while the ICE is still superior (Fig. S8a and Table S4).

Glucose was also used as precursor to produce the glucose-derived carbon dots (GCDs) via the HTC method and compared with the glucose-derived HTC carbon from the solid phase (GHTCs). The same trend also exists when using the carbonized GCDs and GHTCs as anodes in SIBs. Fig. S8b-d present the discharge/charge capacity of carbonized GCDs and GHTCs from 1000 to 1500 °C and the electrochemical properties are shown in Table S5. The carbonized GCDs also have much higher ICE compared to carbonized GHTCs, indicating the universality of this discovery for improved carbon anodes in SIBs by using the carbon dots from the HTC method independently of the carbon source.

Electrochemical impedance spectroscopy (EIS) and XPS were performed to further investigate the SEI formation on CCD1000 and CHTC1000 who have the most apparent difference in ICE. Fig. S9a shows the Nyquist plot of CCD1000 and CHTC1000. Both the spectra display two depressed semi-circles at high and medium frequency regions, corresponding to the resistance of the SEI (R_{SEI}) and charge transfer (R_{CT}), respectively, as well as the liner regions at the low frequency which is attributed to the Warburg impedance.[41–43] The spectra were fitted by using the equivalent circuit shown in Fig. S9b and the calculated R_{SEI} is 3.80 Ω for CCD1000, which is lower than 9.44 Ω for CHTC1000. This could be attributed to reduced SEI formation of CCD1000 than CHTC1000 at the first cycle due to the much smaller surface area and is consistent with the difference in ICE of these two samples. Fig. S10 shows the fitted C1s spectra of pristine and cycled CCD1000 and CHTC1000 after the initial cycle. Both the cycled CCD1000 and CHTC1000 show significantly reduced sp^2 C peaks at around 284.5 eV compared with the pristine samples, indicating the formation of SEI covered on the surface of the electodes.[44] The elements ratio of C/O decreases from 9.9 to 2.1 for pristine and cycled CCD1000 and decreases from 4.7 to 1.3 for CHTC1000 (Fig. S6 and Table S6), which is ascribed to the decomposition of electrolyte with lots of oxygen-contained functional group, leading to higher oxygen content.[45] The higher C/O ratio and less oxygen content of the cycled CCD1000 than CHTC1000 suggests less decomposition of electrolyte and less SEI formation for CCD1000.[45] Furthermore, there are extra peaks appear at around 290 eV in the cycled samples which could be attributed to the -CO_3 group, suggesting the containment of Na_2CO_3 in the SEI.[44–46] The ratio of the -CO_3 group was calculated to be around 6.0% for cycled CCD1000 which is lower than 13.5% for CHTC1000 (Table S5), also implying less SEI formed on the surface of CCD1000.

The cycling capability of carbonized CCDs and CHTCs in half cells is shown in Fig. 5c and Fig. S11. The first five cycles are performed at 30 mA g^{-1} and subsequent cycles are at 150 mA g^{-1}. After 100 cycles, CCD1300 maintains around 96% of its initial capacity, showing an excellent cycling stability which is better than CHTC1300 (82% of retention). However, carbonized CHTCs have relatively better capability at high current densities than carbonized CCDs (Fig. S12) which could be attributed to the less ordered structures and larger

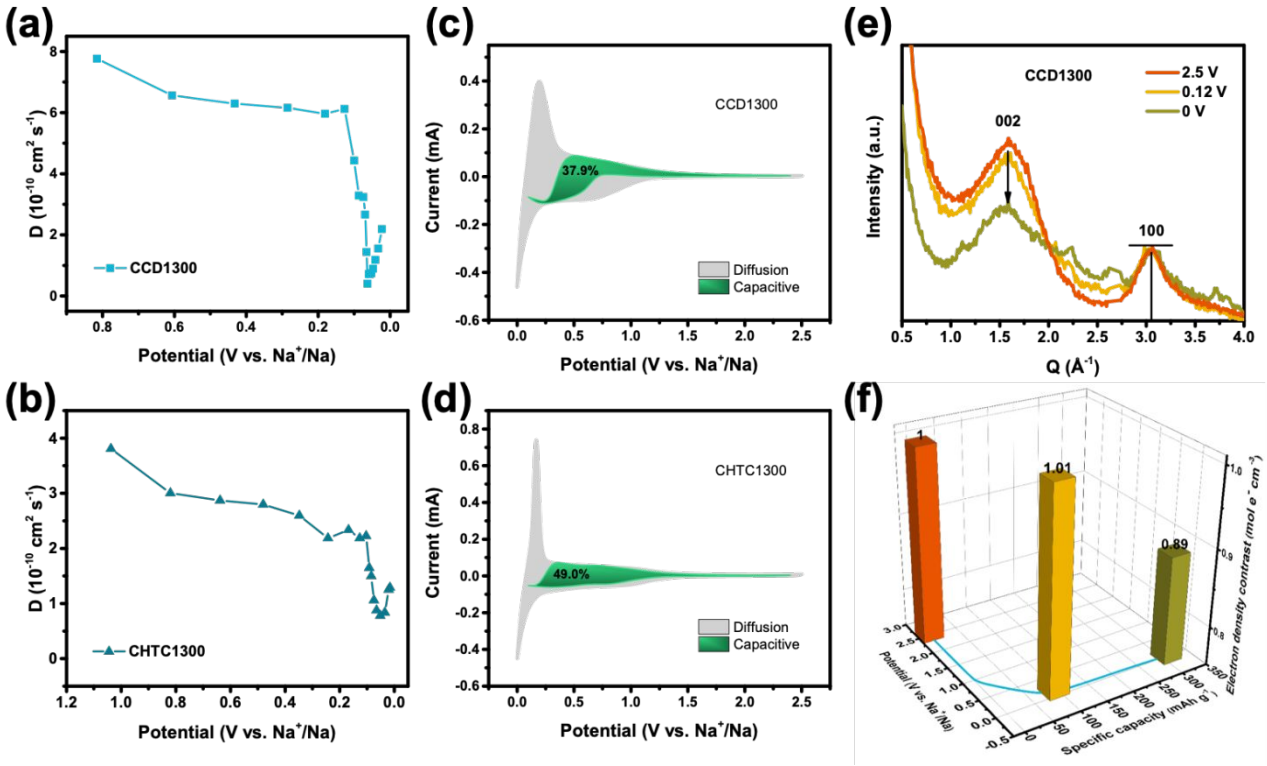

Fig. 6. (a)-(b) Na^+ ions diffusion coefficients from GITT results of CCD1300 and CHTC1300. (c)-(d) CV profiles and corresponding capacitive contribution of CCD1300 and CHTC1300 at 0.2 mV s^{-1}. (e) *Ex situ* WAXS patterns of CCD1300 from 2.5 to 0 V (vs. Na^+/Na) at the second sodiation process. (f) Calculated electron density contrast at different sodiation status of CCD1300.

number of defects in the CHTC samples, leading to longer sloping region in the discharge/charge profiles (Table S3), which is beneficial for faster Na^+ ions transportation.[34] This also implies the fact that it is hard to achieve both high energy density and power density at the same time, which requires further consideration.

To investigate the practical performance of CCD1300, $NaNi_{1/3}Fe_{1/3}Mn_{1/3}O_2$ cathode was used to assemble the coin-type full cell. Fig. 5d-e show the typical charge/discharge curves of $NaNi_{1/3}Fe_{1/3}Mn_{1/3}O_2$//CCD1300 and $NaNi_{1/3}Fe_{1/3}Mn_{1/3}O_2$//CHTC1300 full cells at the current rate of 30 mA g^{-1}. They deliver similar reversible capacities of 283 and 282 mAh g^{-1}, respectively (based on the mass of anodes). However, the energy density of $NaNi_{1/3}Fe_{1/3}Mn_{1/3}O_2$//CCD1300 could reach 248 Wh kg^{-1} (based on the mass of cathode and anode active materials), around 14% higher than that of $NaNi_{1/3}Fe_{1/3}Mn_{1/3}O_2$//CHTC1300, owing to the very long plateau region and small irreversible capacity. Furthermore, due to the much higher ICE and smaller irreversible capacity in the first cycles, CCD1300 requires less cathode material when assembled in full cell, significantly reducing the total cost for future commercialization and also beneficial to the higher energy density. The charge/discharge profiles at various current rates and the cycling stability of the full cells are shown in Fig. S13. $NaNi_{1/3}Fe_{1/3}Mn_{1/3}O_2$//CCD1300 full cell could deliver 195 and 134 mAh g^{-1} at 600 and 1200 mA g^{-1}, respectively, and retains 213 mAh g^{-1} after 100 cycles at 60 mA g^{-1}.

Sodium storage mechanism

The capacity of the sloping region above 0.12 V (vs. Na^+/Na) of all the resulting carbons is shown in Table S3. Both carbonized CCDs and CHTCs show a decrease in the sloping capacity with increased carbonization temperatures, and at each temperature, carbonized CCDs have lower sloping capacity than CHTC. This could be correlated with the aforementioned characterizations that CCD always have more ordered nanodomains and fewer defects than the carbonized CHTCs at the same temperature, and to the fact that higher carbonization temperatures also leads to such a trend, suggesting that the sloping region could be attributed to the adsorption of Na^+ ions on the defect sites of the carbon materials. Fig. S14 and Fig. 6a-b present the galvanostatic intermittent titration technique (GITT) results of CCD1300 and CHTC1300, showing the phenomenon that the Na^+ ions diffuse much faster in the sloping region compared to the plateau region, which could be attributed to the capacitive adsorption behavior in the sloping region requiring less energy than the redox reaction at the plateau region.[26,32] Cyclic voltammetry (CV) at different scan rates was performed and the corresponding capacitive contributions were calculated for CCD1300 and CHTC1300 at 0.2 mV s^{-1} (Fig. S15 and Fig. 6c-d). CCD1300 shows approximately 38% of capacitive contribution which is lower than 49% for CHTC1300 at the same scan rates, indicating that fewer capacitive reactions happen for CCD1300 with smaller sloping capacity. All of these analyses are consistent with the above conclusion that Na^+ ions adsorb at the defect sites on the surface within the sloping region.

Ex situ wide angle X-ray scattering (WAXS) was investigated to further study the sodium storage mechanism of CCD1300. Fig. 4e shows the *ex situ* WAXS patterns of the second sodiation process from 2.5 to 0 V (vs. Na^+/Na) with the (100) peaks normalized to the same height. There is no apparent (002) peak position shift during the whole discharge procedure, suggesting that no obvious graphitic interlayer insertion occurs. Furthermore, the relative intensity of the (002) peaks shows almost no drop from 2.5 to 0.12 V (vs. Na^+/Na) in the sloping region, while a huge decrease is apparent from 0.12 to 0 V (vs. Na^+/Na) in the plateau region. This might be attributed to the destructive interference of X-ray scattering caused by the Na^+ ions filling into the nanovoids formed between the turbostratic nanodomains and interacting with the surface of (002) planes, which changes the atomic structures.[47] These results are also consistent with the ex situ SAXS results fitted by the modified Porod method (Fig. S16).[22] The calculated electron density contrast $\Delta\rho$ between nanopores and the carbon matrix shows no change in the sloping region and a drop from 1.01 to 0.89 mol e^- cm^{-3} during the plateau region (Fig. 6f), suggesting that the nanopore filling happens only at the plateau region.

Discussion

Although the formation mechanism of hydrothermal carbon dots is still unclear, it is likely that the small nanodomains or nanoparticles with local graphitic nanostructures form on an amorphous carbon matrix during the HTC process, which could be retained even after further carbonization. According to the above characterizations, carbonized CCDs and CHTCs are normally amorphous carbons but the carbonized CCDs have localized domains of high crystallinity and relatively more ordered structures, fewer defects and lower specific surface area. The low surface area is beneficial for suppressing the SEI formation and decreasing the irreversible capacity, and the relatively higher graphitization degree and fewer defects also reduce the irreversible reactions during the first cycles and enhance the ICE. It is well known that hard carbons with disordered structures are ideal candidates as anode materials for SIBs compared to soft carbons and graphite, however, the disordered structures and defects would also cause irreversible reactions.[35] Therefore, as too disordered structures or too many defects in hard carbon materials could also limit the reversibility, it is worth considering in the future to balance the sodium storage sites with irreversible reactions when designing high-performance carbon anodes for SIBs.

The carbon dots from the supernatant of the HTC process is usually discarded and ignored as waste, so the discovery of the high-ICE anode materials could be an additional value when using HTC to produce carbonaceous materials for SIBs. Since the carbon dots from the supernatant and the hydrochars from the sediment have different sodium storage performance (the carbon dots-derived carbons have higher energy density while the hydrochars-derived carbons have better rate capability), they might be promising to be used in different market after future optimization and commercialization (i.e the carbon dots-derived electrodes could be used in the market requires higher energy density and the hydrochars-derived electrodes could be used for faster charging).

The sodium storage mechanism of CCD1300 could be summarized as an adsorption-filling model where the Na^+ ions adsorb at defect sites in the sloping region and fill into nanovoids at the plateau region, which is consistent with many previous studies.[20,25,38,48]

However, we do believe that the sodium storage mechanism may vary for different carbon materials due to the different microstructures. The lowest energy of Na^+ ion storage site is expected to be highly dependent on the balance between different structural parameters such as d-spacing, pore volume and size, and defect concentration, and therefore the mechanisms of sodium storage in the carbon will differ accordingly. In addition, the *ex situ* experiments have their limitations as artifacts from sample handling can affect the obtained results. Therefore, this difficult task of understanding clearly the sodium storage mechanism in carbonaceous materials still needs further consideration. The carbonized CCDs and CHTCs might be an ideal option to have a deeper investigation of sodium storage mechanism on account of their same source and synthesis method but different nanostructures, which is helpful to have clear structure-mechanism correlations in the future.

Conclusions

We have utilized carbon dots from the supernatant of the HTC process to make superior anodes for SIBs. Compared to the carbonized HTC carbon spheres when normally HTC is employed to convert biomass into carbons and used as anodes for SIBs, the carbonized carbon dots show an increased ICE up to 91% which is one of the highest values reported for carbonaceous anodes in SIBs. The high sodium storage capacity, large ratio of plateau regions in the discharge/charge profiles as well as the extensively reduced irreversible capacity due to the more ordered structures, fewer defects and lower surface area means that the carbonized CCD anodes require a much smaller amount of expensive cathode material to balance the full cell, which could significantly enhance the energy density and reduce the total cost. The energy density of $NaNi_{1/3}Fe_{1/3}Mn_{1/3}O_2$//CCD1300 full cell could reach 248 Wh kg^{-1}, which is much higher than that of the CHTC1300. This discovery also has its universality for other biomass, making the ignored treasure from “the waste” of HTC process a great potential for future commercialization and provides a new aspect of designing high-performance carbon anodes for SIBs.

Conflicts of interest

There are no conflicts to declare.

Acknowledgements

The authors would like to thank Dr. Gavin Stenning for the help on the NanoInXider instrument at ISIS Neutron and Muon Source. M. -M. T. would like to thank Engineering and Physical Sciences Research Council (EPSRC) for the research funding (EP/R021554/1; EP/S018204/1). F. X., Z. X., H. L. and Z. G. thank the China Scholarship Council (CSC) for the scholarship.

Notes and references

1 H. Zhu, W. Luo, P. N. Ciesielski, Z. Fang, J. Y. Zhu, G. Henriksson, M. E. Himmel and L. Hu, *Chem. Rev.*, 2016, **116**, 9305–9374.

2 J. Ding, W. Hu, E. Paek and D. Mitlin, *Chem. Rev.*, 2018, **118**, 6457–6498.

3 L. Mu, S. Xu, Y. Li, Y. S. Hu, H. Li, L. Chen and X. Huang, *Adv. Mater.*, 2015, **27**, 6928–6933.

4 H. Yamamoto, S. Muratsubaki, K. Kubota, M. Fukunishi, H. Watanabe, J. Kim and S. Komaba, *J. Mater. Chem. A*, 2018, **6**, 16844–16848.

5 Y. Zheng, Y. Wang, Y. Lu, Y. S. Hu and J. Li, *Nano Energy*, 2017, **39**, 489–498.

6 H. He, D. Sun, Y. Tang, H. Wang and M. Shao, *Energy Storage Mater.*, , DOI:10.1016/j.ensm.2019.05.008.

7 H. Yu, R. Shi, Y. Zhao, G. I. N. Waterhouse, L. Z. Wu, C. H. Tung and T. Zhang, *Adv. Mater.*, 2016, **28**, 9454–9477.

8 H. Zhang, H. Huang, H. Ming, H. Li, L. Zhang, Y. Liu and Z. Kang, *J. Mater. Chem.*, 2012, **22**, 10501–10506.

9 A. Marinovic, L. S. Kiat, S. Dunn, M.-M. Titirici and J. Briscoe, *ChemSusChem*, 2017, **10**, 1004–1013.

10 J. Briscoe, A. Marinovic, M. Sevilla, S. Dunn and M. Titirici, *Angew. Chemie - Int. Ed.*, 2015, **54**, 4463–4468.

11 H. Hou, C. E. Banks, M. Jing, Y. Zhang and X. Ji, *Adv. Mater.*, 2015, **27**, 7861–7866.

12 M.-M. Titirici and M. Antonietti, *Chem. Soc. Rev.*, 2010, **39**, 103–116.

13 M.-M. Titirici, R. J. White, N. Brun, V. L. Budarin, D. S. Su, F. del Monte, J. H. Clark and M. J. MacLachlan, *Chem. Soc. Rev.*, 2015, **44**, 250–290.

14 M. M. Titirici, R. J. White, C. Falco and M. Sevilla, *Energy Environ. Sci.*, 2012, **5**, 6796–6822.

15 N. Papaioannou, A. Marinovic, N. Yoshizawa, A. E. Goode, M. Fay, A. Khlobystov, M. M. Titirici and A. Sapelkin, *Sci. Rep.*, 2018, **8**, 1–10.

16 Q. Liang, W. Ma, Y. Shi, Z. Li and X. Yang, *Carbon N. Y.*, 2013, **60**, 421–428.

17 Y. Li, S. Xu, X. Wu, J. Yu, Y. Wang, Y. S. Hu, H. Li, L. Chen and X. Huang, *J. Mater. Chem. A*, 2015, **3**, 71–77.

18 L. Xiao, H. Lu, Y. Fang, M. L. Sushko, Y. Cao, X. Ai, H. Yang and J. Liu, *Adv. Energy Mater.*, 2018, **1703238**, 1–7.

19 K. Tang, L. Fu, R. J. White, L. Yu, M. Titirici, M. Antonietti and J. Maier, *Adv. Energy Mater.*, 2012, 873–877.

20 D.-S. Bin, Y. Li, Y.-G. Sun, S.-Y. Duan, Y. Lu, J. Ma, A.-M. Cao, Y.-S. Hu and L.-J. Wan, *Adv. Energy Mater.*, 2018, **1800855**, 1800855.

21 H. Wang, W. Yu, J. Shi, N. Mao, S. Chen and W. Liu, *Electrochim. Acta*, 2016, **188**, 103–110.

22 D. A. Stevens and J. R. Dahn, *J. Electrochem. Soc.*, 2000, **147**, 4428–4431.

23 X. Ma, C. Yuan and X. Liu, *Materials (Basel).*, 2014, **7**, 75–84.

24 X. Yan, Y. Yang, Y.-S. He, X.-Z. Liao, H. Wang and Z.-F. Ma, *J. Electrochem. Soc.*, 2016, **163**, A565–A570.

25 Y. Li, Y. S. Hu, M. M. Titirici, L. Chen and X. Huang, *Adv. Energy Mater.*, 2016, **6**, 1600659.

26 C. Bommier, T. W. Surta, M. Dolgos and X. Ji, *Nano Lett.*, 2015, **15**, 5888–5892.

27 P. Lu, Y. Sun, H. Xiang, X. Liang and Y. Yu, *Adv. Energy*

Mater., 2018, **8**, 1–8.

28 V. Augustyn, P. Simon and B. Dunn, *Energy Environ. Sci.*, 2014, **7**, 1597–1614.

29 C. Falco, N. Baccile and M. Titirici, *Green Chem.*, 2011, **13**, 3273–3281.

30 Z. Li, C. Bommier, Z. Sen Chong, Z. Jian, T. W. Surta, X. Wang, Z. Xing, J. C. Neuefeind, W. F. Stickle, M. Dolgos, P. A. Greaney and X. Ji, *Adv. Energy Mater.*, 2017, **7**, 1–10.

31 A. C. Ferrari and D. M. Basko, *Nat. Nanotechnol.*, 2013, **8**, 235–246.

32 F. Xie, Z. Xu, A. C. S. Jensen, H. Au, Y. Lu, V. Araullo-Peters, A. J. Drew, Y.-S. Hu and M.-M. Titirici, *Adv. Funct. Mater.*, 2019, 1901072.

33 Z. Wang, L. Qie, L. Yuan, W. Zhang, X. Hu and Y. Huang, *Carbon N. Y.*, 2013, **55**, 328–334.

34 Y. Qi, Y. Lu, F. Ding, Q. Zhang, H. Li, X. Huang, L. Chen and Y.-S. Hu, *Angew. Chemie - Int. Ed.*, 2019, **131**, 4405–4409.

35 X. Zhao, Y. Ding, Q. Xu, X. Yu, Y. Liu and H. Shen, *Adv. Energy Mater.*, 2019, **1803648**, 1803648.

36 X. Dou, I. Hasa, D. Saurel, C. Vaalma, L. Wu, D. Buchholz, D. Bresser, S. Komaba and S. Passerini, *Mater. Today*, 2019, **23**, 87–104.

37 Z. Xu, F. Xie, J. Wang, H. Au, M. Tebyetekerwa, Z. Guo, S. Yang, Y. Hu and M. Titirici, *Adv. Funct. Mater.*, 2019, **1903895**, 1903895.

38 J. Ding, H. Wang, Z. Li, A. Kohandehghan, K. Cui, Z. Xu, B. Zahiri, X. Tan, E. M. Lotfabad, B. C. Olsen and D. Mitlin, *ACS Nano*, 2013, **7**, 11004–11015.

39 C. Bommier, D. Mitlin and X. Ji, *Prog. Mater. Sci.*, 2018, **97**, 170–203.

40 C. Matei, J. Górka, V. Simone, L. Simonin, S. Martinet and C. Vix-guterl, *Nano Energy*, 2018, **44**, 327–335.

41 S. J. R. Prabakar, J. Jeong and M. Pyo, *Electrochim. Acta*, 2015, **161**, 23–31.

42 L. Xiao, Y. Cao, W. A. Henderson, M. L. Sushko, Y. Shao, J. Xiao, W. Wang, M. H. Engelhard, Z. Nie and J. Liu, *Nano Energy*, 2016, **19**, 279–288.

43 H. Lu, X. Chen, Y. Jia, H. Chen, Y. Wang, X. Ai, H. Yang and Y. Cao, *Nano Energy*, 2019, **64**, 103903.

44 S. Komaba, W. Murata, T. Ishikawa, N. Yabuuchi and T. Ozeki, *Adv. Funct. Mater.*, 2011, **21**, 3859–3867.

45 F. A. Soto, P. Yan, M. H. Engelhard, A. Marzouk, C. Wang, G. Xu, Z. Chen, K. Amine, J. Liu, V. L. Sprenkle, F. El-Mellouhi, P. B. Balbuena and X. Li, *Adv. Mater.*, 2017, **29**, 1606860.

46 Y. Pan, Y. Zhang, B. S. Parimalam, C. C. Nguyen, G. Wang and B. L. Lucht, *J. Electroanal. Chem.*, 2017, **799**, 181–186.

47 D. A. Stevens and J. R. Dahn, *J. Electrochem. Soc.*, 2001, **148**, A803.

48 Y. Cao, L. Xiao, M. L. Sushko, W. Wang, B. Schwenzer, J. Xiao, Z. Nie, L. V. Saraf, Z. Yang and J. Liu, *Nano Lett.*, 2012, **12**, 3783–3787.